Negative refractive index in optics of metal–dielectric composites

Alexander V. Kildishev, Wenshan Cai, Uday K. Chettiar, Hsiao-Kuan Yuan, Andrey K. Sarychev, Vladimir P. Drachev, and Vladimir M. Shalaev

School of Electrical and Computer Engineering, Purdue University, 465 Northwestern Avenue, West Lafayette, Indiana 47907

Received September 13, 2005; accepted September 22, 2005; posted November 29, 2005 (Doc. ID 64771)

Specially designed metal–dielectric composites can have a negative refractive index in the optical range. Specifically, it is shown that arrays of single and paired nanorods can provide such negative refraction. For pairs of metal rods, a negative refractive index has been observed at 1.5 μm. The inverted structure of paired voids in metal films can also exhibit a negative refractive index. A similar effect can be accomplished with metal strips in which the refractive index can reach −2. The refractive index retrieval procedure and the critical role of light phases in determining the refractive index are discussed. © 2006 Optical Society of America

OCIS codes: 160.4760, 260.5740, 310.6860.

1. INTRODUCTION

In recent years, there has been a strong interest in novel optical media that have become known as left-handed materials (LHMs) or negative-index materials (NIMs). Such materials have not been discovered as natural substances or crystals but rather are artificial, man-made materials. The optical properties of such media were considered in early papers by two Russian physicists, Mandel'shtam[1,2] and Veselago,[3] although much earlier works on negative phase velocity and its consequences belong to Lamb[4] (in hydrodynamics) and Schuster[5] (in optics).

In NIMs, $\mathbf{k}$, $\mathbf{E}$, and $\mathbf{H}$ form a left-handed set of vectors and were therefore named LHMs by Veselago. As a result of the negative index of refraction and negative phase velocity, these artificial materials exhibit a number of extraordinary features, including an inverse Snell's law relationship, a reversed Doppler shift, and reversed Cherenkov radiation. These features suggest a flexible regulation of light propagation in these media and facilitate new, fascinating applications.

The most recent successful efforts to demonstrate negative refraction have been inspired by Pendry's revision[6] of the Veselago lens, which renewed interest in the practical aspects of the earlier papers. Pendry predicted that a NIM lens can act as a superlens by providing spatial resolution beyond the diffraction limit. Figure 1 compares the simplest case of refraction at a single interface between vacuum and a common, positive-refractive-index material [Fig. 1(a)] versus refraction at the interface with a NIM [Fig. 1(b)]. For any oblique angle of incidence θ_i, the tangential wave vector $\mathbf{k}_{\parallel}$ of an incident plane wave from the vacuum side must remain continuous across the interface. This is the case for both positive and negative refractive indices. However, in contrast to a normal, positive-refraction material, the wave-vector component normal to the interface ($\mathbf{k}_{\perp}$) must change the sign, as the light passes from vacuum into a NIM. As a result, the total refracted wave vector is on the same side of the normal as the incident wave vector. Figure 1(b) illustrates this effect as the reversed Snell's law, where the angles of reflection (θ_r) and transmission (θ_t) are reversed ($\theta_r = \theta_t$) for the case of $n=-1$. This reversal suggests insightful consequences for the imaging applications of NIMs, the most critical of which is the perfect lens as illustrated in Fig. 1(c). For refracted rays from a point source, a planar NIM slab of sufficient thickness with $n=-1$ should first focus the rays inside the NIM and then refocus them again behind the slab. At the perfect lensing condition of $n=-1$, this focusing property is extraordinary, and the resolution limit intrinsic to conventional imaging no longer applies to imaging with a NIM slab as shown by Pendry.[6] The essence of the effect is that a NIM compensates for the usual decay of the evanescent waves. In contrast to a conventional imaging device, in a superlens these evanescent waves are recovered by the NIM, and the image is perfectly reconstructed.[6] The perfect lensing requirements [$\mathrm{Re}(n)=-1$, $\mathrm{Im}(n)=0$] are difficult conditions to meet. The first requirement means that n is wavelength dependent and the perfect lens is restricted to work at a single wavelength. The second requirement implies that there is no absorption in the NIM. In reality, losses are always present in the NIM and can dramatically diminish the resolution.[7,8]

The development of optical NIMs is closely connected to studies of periodic arrays of elementary scatterers, in which, for example, frequency-selective surfaces (FSSs) arranged from those arrays have been used as narrow-band filters for plane waves. The major resonant elements of optical metal–dielectric composites (metallic spheres, disks, rods, and their inversions, i.e., circular and elliptic holes) have been inherited from earlier FSS designs, together with evident orthotropic properties and angular dependences. Another source of earlier expertise is found in the studies of artificial dielectrics (ADs), in which the homogenization method and approaches to define equivalent electromagnetic material properties have been exam-

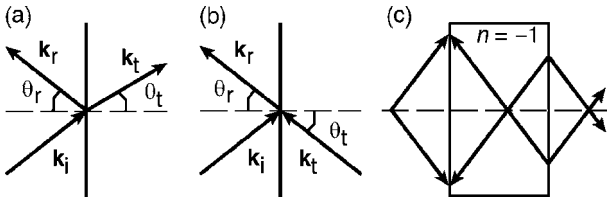

Fig. 1. (a) Snell's law at an interface between vacuum and a positive-refractive-index material, (b) reversed Snell's law at the interface with NIM ($n=-1$), and (c) the superlens.

ined under resonant conditions. Predictions of anomalously large effective permeability and permittivity due to resonant regimes of elementary scatterers have also been made for ADs arranged from periodic metal–dielectric structures.[9]

Although negative permittivity in the optical range is easy to attain for metals, there is no magnetic response for naturally occurring materials at such high frequencies. Recent theories and experiments showed that a magnetic response and negative permeability can be accomplished in the terahertz spectral ranges by using parallel rods, split-ring resonators, and other structures.[10–15] As predicted[14] and experimentally demonstrated,[15] u-shaped structures are particularly well suited for magnetism at optical frequencies. Recently, light propagation through an interface that mimics negative refraction has also been found in two-dimensional (2D) photonic crystals[16] (PCs). It has been shown that, under certain conditions, unique focusing effects in PCs are also possible.[17]

Up to the microwave frequencies the fabrication of metal–dielectric composites can follow practically any pattern suggested by either human intuition or computer-aided tools with evolutionary optimization. Yet at optical frequencies, the best possible design of metal–dielectric composite NIM should overcome two substantial difficulties: severe fabrication constraints and increased losses. For these reasons, this paper addresses the simplest geometries of resonant 3D structures. Such structures include coupled metal rods in a dielectric host[18–22] (fabricated, for example, through electron-beam lithography) and inversions of rods, i.e., coupled dielectric holes of elliptical (spherical,[23] in the limiting case) or rectangular shape[24] (fabricated, for example, by etching trilayer metal–dielectric–metal films using ion-beam etching or through interferometric lithography).

The first experimental realization of a negative refractive index in the optical range (at 1.5 μm) was accomplished with paired metal nanorods in a dielectric[22] and then for the inverted system of paired dielectric voids in a metal.[23,24] We note that inverted NIMs, i.e., elliptical or rectangular dielectric voids in metal films,[24] are physically equivalent to paired metal rods in a dielectric host, in accordance with the Babinet principle.[25] We also note here Ref. 26, which considers other interesting optical properties of metal rods, although these properties are not related directly to NIMs.

In the current paper, in addition to paired metal rods and dielectric voids, we also study 2D coupled-strip composites as a basis for further comprehensive studies of NIMs.

2. HOMOGENIZED OPTICAL PARAMETERS OF NIMS

A. Equivalent Multilayer Structure at Normal Incidence

Our NIM designs are confined in a thin layer placed on a thick substrate; therefore, a direct measurement cannot resolve the reversed refraction owing to insufficient optical length. Fortunately, accurate indirect measurements work well to retrieve the effective optical constants of the NIM.

First, we ascribe an effective refractive index to a layer of the NIM as if it were a layer of a homogeneous medium. This assumption suggests that the periodic structure of NIM does not diffract the incident plane wave. Then we consider a straightforward direct problem of plane-wave propagation through a multilayer structure of homogeneous materials at normal incidence, as shown in Fig. 2. The electric field at the initial interface on the source side ($E_i=E_{i,1}$) is first compared with the field transmitted through the same boundary ($E^-=E_{t,1}$) and then compared with the transmitted field ($E^+=E_{t,\nu_{\max}}$) at the last interface of the back side. Then, provided that the multilayer structure is surrounded by vacuum (i.e., $n_0=n_{\nu_{\max}}=1$), the complex reflection coefficient $r=E^-/E_i-1$ and the transmission coefficient $t=E^+/E_i$ of the entire structure can be obtained from the following equations:

$$t=\frac{2}{z_{11}+z_{12}+z_{21}+z_{22}}, \tag{1}$$

$$r=\frac{(z_{11}+z_{12})-(z_{21}+z_{22})}{z_{11}+z_{12}+z_{21}+z_{22}}. \tag{2}$$

Here z_{11},z_{12},z_{21}, and z_{22} are the elements of the total characteristic matrix ($\mathbf{Z}$) of a given multilayer structure obtained as the matrix product of the individual characteristic matrices of each layer, i.e.,

$$\mathbf{Z}=\prod_{\nu=1}^{\max(\nu)}\mathbf{Z}_\nu. \tag{3}$$

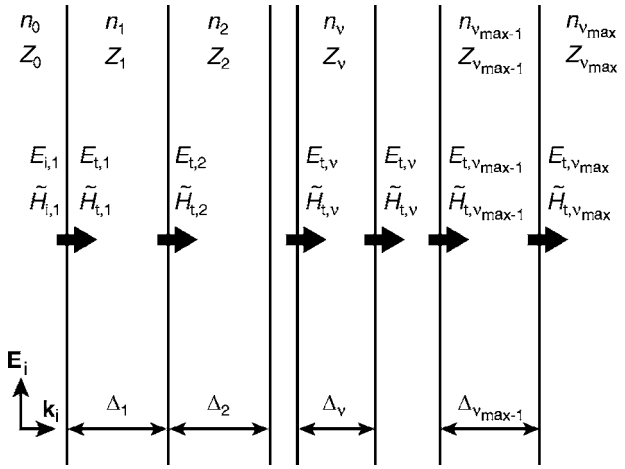

Fig. 2. Multilayer structure illuminated from left to right by a monochromatic plane wave at normal incidence. Each layer is made of a homogeneous material and characterized by refractive index (n), impedance (Z), and thickness (Δ).

Provided that for each layer the relative bulk material properties (ϵ_ν and μ_ν) and therefore the refractive index ($n_\nu=\sqrt{\epsilon_\nu\mu_\nu}$) and intrinsic impedance ($Z_\nu=\sqrt{\mu_\nu/\epsilon_\nu}$) are known, the characteristic matrix of the given layer is defined as

$$\mathbf{Z}_\nu=\begin{bmatrix}\cos(n_\nu k\Delta_\nu) & -\imath Z_\nu\sin(n_\nu k\Delta_\nu)\\ -\imath Z_\nu^{-1}\sin(n_\nu k\Delta_\nu) & \cos(n_\nu k\Delta_\nu)\end{bmatrix}, \tag{4}$$

where Δ_ν is the thickness of the νth layer. As a result, similar to Ref. 27, for a single layer in vacuum, we have a remarkably symmetric pair of equations:

$$\cosh\zeta=(1-t^2+r^2)/(2r), \tag{5}$$

$$\cos N=(1-r^2+t^2)/(2t), \tag{6}$$

where $\zeta\triangleq 2\coth^{-1}Z$ and $N=nk\Delta$.

If the refractive indices of a source-side medium and a back-side medium differ from that of vacuum, then using normalized values of the magnetic field intensity $\tilde{H}=(\mu_0/\epsilon_0)^{1/2}H$ and defining the electric transmission coefficient ($t_{E,\nu}=E_{t,\nu}/E_{i,1}$) in addition to the magnetic transmission coefficient ($t_{H,\nu}=\tilde{H}_{t,\nu}/E_{i,1}$), we arrive at a matrix identity for a given layer:

$$\begin{pmatrix}t_{E,\nu}\\ t_{H,\nu}\end{pmatrix}=\mathbf{Z}_\nu\begin{pmatrix}t_{E,\nu+1}\\ t_{H,\nu+1}\end{pmatrix}. \tag{7}$$

In our case, the only unknown parameters in the entire multilayer structure are those of the NIM ($n_{\mathrm{NIM}}=n_\nu$ and $Z_{\mathrm{NIM}}=Z_\nu$), and the above equation can be inverted to restore the parameters through a set of equations:

$$Z_\nu^2=(t_{E,\nu}^2-t_{E,\nu+1}^2)/(t_{H,\nu}^2-t_{H,\nu+1}^2), \tag{8}$$

$$n_\nu=N_\nu/(k\Delta_\nu), \tag{9}$$

where

$$N_\nu=\cos^{-1}\left(\frac{t_{E,\nu}t_{H,\nu}+t_{E,\nu+1}t_{H,\nu+1}}{t_{E,\nu}t_{H,\nu+1}+t_{E,\nu+1}t_{H,\nu}}\right). \tag{10}$$

We assume that the coefficients t_E and t_H are known from both sides of the layer, either from calculations or through measurements.

B. Restoration of the Refractive Index

Although, Eqs. (8) and (9) seem quite straightforward, physically sound restrictions should be applied to both expressions.[27] Since the material of the νth layer is passive, we choose appropriate signs in Eqs. (8) and (9) in order to obey the restrictions $\mathrm{Re}(Z)>0$ and $\mathrm{Im}(n)>0$. Thus, the refractive index $n_\nu=n'_\nu+\imath n''_\nu$ is given by

$$n'_\nu=[\mathrm{sign}(N''_\nu)N'_\nu+2\pi l]/(k\Delta_\nu), \tag{11}$$

$$n''_\nu=\mathrm{sign}(N''_\nu)N''_\nu/(k\Delta_\nu), \tag{12}$$

where $\mathrm{sign}(x)$ is equal to 1 if $x\geqslant 0$ and to -1 otherwise; $N'_\nu=\mathrm{Re}(N_\nu)$ and $N''_\nu=\mathrm{Im}(N_\nu)$.

Since n' has multiple branches, to avoid ambiguities in selecting a phase-adjusting integer l in Eq. (11), one should start the restoration of n'_ν from a higher wavelength (far away from resonances) and obtain physically sound values of n'_ν. Then one should move the wavelength toward smaller values while simultaneously adjusting the values of l in Eq. (11) to obtain a continuous behavior for n'_ν. For achieving accurate and unambiguous results, the restored layer should be much thinner than (at least) the longest wavelength in the sweep range, and the sweep step size should be adaptively decreased at resonances to provide an adequate number of points in steep segments.

In Eqs. (8)–(12), the coefficients $t_{E,\nu}, t_{E,\nu+1}$ and $t_{H,\nu}$, $t_{H,\nu+1}$ are considered to be known at both sides of the layer. These coefficients can be recursively restored through Eq. (7) by either direct propagation or backpropagation.

Consider, for example, the most frequent cases shown in Fig. 3, where Fig. 3(a) depicts a NIM layer in air ($n_0=n_2=1$); Fig. 3(b) shows a NIM layer on thick glass ($n_0=1$, $n_2=n_s$, with n_s as the refractive index of glass); and Fig. 3(c) shows a NIM layer on an indium tin oxide–(ITO-) coated glass substrate ($n_0=1$, $n_3=n_s$, and $n_2=n_{\mathrm{ITO}}$). The refractive index of a single NIM layer in air[27] with

$$t_{E,1}=1+r,\quad t_{H,1}=1-r, \tag{13}$$

and $t_{E,2}=t_{H,2}=t$ is already given by Eqs. (5) and (6).

The NIM–air interface coefficients $t_{E,1}$ and $t_{H,1}$ of a NIM layer on a thick bare glass substrate [Fig. 3(b)] are also defined by Eqs. (13), but the coefficients at the NIM–substrate interface are given by $t_{E,2}=t$ and $t_{H,2}=n_st$, i.e.,

$$N_1=\cos^{-1}\left[\frac{1-r^2+n_st^2}{(n_s+1)t+rt(n_s-1)}\right], \tag{14}$$

where t is evaluated in the substrate.

Coefficients $t_{E,1}$ and $t_{H,1}$ at the NIM–air interface of a NIM layer on an ITO–glass substrate as in Fig. 3(c) are also defined by Eqs. (13), but back-side coefficients should be first calculated (measured) in the substrate at the ITO–glass interface ($t_{E,3}=t$, $t_{H,3}=n_st$) and then backpropagated by using Eq. (7), i.e.,

$$\begin{pmatrix}t_{E,2}\\ t_{H,2}\end{pmatrix}=\mathbf{Z}_2\begin{pmatrix}t\\ n_st\end{pmatrix}, \tag{15}$$

where

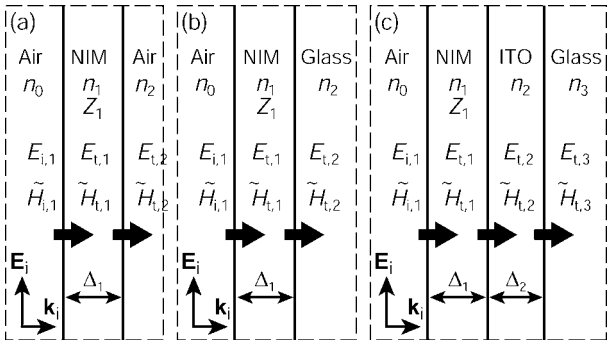

Fig. 3. (a) NIM layer in air ($n_0=n_2=1$), (b) a single NIM layer on a bare glass substrate ($n_0=1$, $n_2=n_s$), and (c) a NIM layer on an ITO–glass substrate ($n_0=1$, $n_2=n_{\mathrm{ITO}}$, $n_3=n_s$).

$$\mathbf{Z}_2 = \begin{bmatrix} \cos(n_2 k\Delta_2) & -\imath n_2^{-1}\sin(n_2 k\Delta_2) \\ -\imath n_2 \sin(n_2 k\Delta_2) & \cos(n_2 k\Delta_2) \end{bmatrix},$$

with $n_2 = n_{\mathrm{ITO}}$. For all cases in Fig. 3, the values of n'_1 and n''_1 are finally calculated by using Eqs. (10)–(12) for $\nu = 1$.

C. Phase-based Approximations of the Refractive Index

Consider the simple NIM structure depicted in Fig. 4(a). The NIM consists of a periodic array of identical gold strips separated by a silica spacer. The array is periodic in the vertical direction, and its simple geometry is characterized by a period h, a gold-strip width w, a strip thickness δ, and a total NIM layer thickness Δ_1. Figure 4(b) shows the transverse magnetic field H_y between the strips calculated using the finite-element method (FEM) for two samples with different gold thicknesses (13 and 19 nm). All other dimensions in both case are identical ($h = 480$ nm, $w = 450$ nm, and $\Delta_1 = 160$ nm). The values of H_z in both field maps of Fig. 4(b) are normalized by the instantaneous magnitude of the incident field, which is adjusted to arrive at a positive maximum halfway between the strips. The magnetic field in both cases is calculated at a minimal refractive index (i.e., at $\lambda \approx 850$ nm for $\delta = 13$ nm and $\lambda \approx 900$ nm for $\delta = 19$ nm) and is normalized using the maximal incident field. Figures 4(c) and 4(d) depict the reflectance R, absorbance A, and the refractive index n' of the strips as functions of the wavelength of incident light.

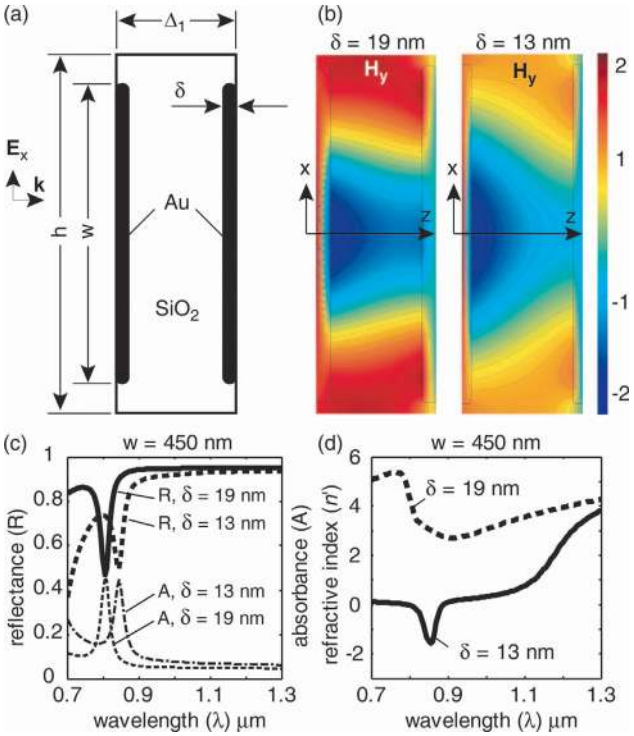

Fig. 4. (a) Cross-section view of a NIM layer arranged from coupled gold strips separated by a layer of silica. The strips are infinite along the y axis (which is perpendicular to the cross-section plane). (b) Transverse magnetic field (H_y) between the strips (for two different thicknesses of gold) for linear E_x polarization of the incident field. (c) and (d) Reflectance (R), absorbance (A), and the refractive index (n') of the strips versus the wavelength of the incident light.

The simulations indicate that the index of refraction for the structure in Fig. 4(a) depends dramatically on thickness δ. Notice how a 6 nm increase in thickness (about 30%) weakens the effective diamagnetic properties of the structure [Fig. 4(b)] and cancels the negative-refraction effect in Fig. 4(d), simultaneously shifting the resonances of A and R toward shorter wavelengths in Fig. 4(c). The quantitative changes in absorbed and reflected energy are to be expected, and an analysis in terms of reflectivity and transmission is sometimes used to restore the refractive index.[23] Unfortunately, these quantitative differences can be easily distorted by experiment–simulation mismatches and measurement errors. The use of only the magnitude changes of reflectivity and transmission complicates the examination of the resonant behavior of n, which, for the most part, follows phase changes in the transmitted and reflected light. Figure 4 clearly shows that structures with similar magnitudes of reflectance (transmittance) may have dramatically different refractive indices, which emphasizes the role of phase measurements in finding the refraction.

To show just how indicative the phase changes can be to the negative-refraction behavior, we consider the following two phase-based approximations for n':

$$n' \approx \frac{\arg t}{k\Delta} = \frac{\tau}{k\Delta} \quad (|r| \ll 1), \tag{16}$$

$$n' \approx \psi = \frac{\left(\arg t - \arg r - \frac{\pi}{2}\right)}{k\Delta} \quad (|r| \to 1), \tag{17}$$

which are obtained from Eq. (6) for either low or large reflectance. For example, taking Eq. (6) at the limit of $|r| \ll 1$ and using $t = \exp[\imath(\tau - \imath \ln|t|)]$, we arrive at expression (16), and the approximation for the imaginary part follows as $n'' \approx \ln|t|/(k\Delta)$. It is interesting to note that, according to expressions (16) and (17), the refractive index is fully determined by phases only, in the corresponding limiting cases.

To provide a test example for expressions (16) and (17), we approximate the values of refractive index obtained from FEM simulations of the 2D structure of Fig. 4(a). Figure 5 depicts the refractive index of periodic paired strips retrieved from the exact retrieval formula of Eq. (6) and independently obtained from the approximate formulas of expressions (16) and (17) for six different geometries. First, note that the negative refractive index can reach large magnitudes for such structures close to −2 [see Figs. 5(e) and 5(f)]. Common parameters for all cases are the period ($h = 480$ nm) and the total layer thickness ($\Delta = 140$ nm). The strips in Figs. 5(a), 5(c), and 5(e) are 440 nm wide and 16, 15, and 14 nm thick, respectively. The 450 nm strips in Figs. 5(b), 5(d), and 5(f) are 17, 16, and 15 nm thick, respectively. To simulate the complex permittivity of gold in FEM models, we use the Drude model with parameters selected to match the experimental optical constants of bulk gold. Each simulation begins

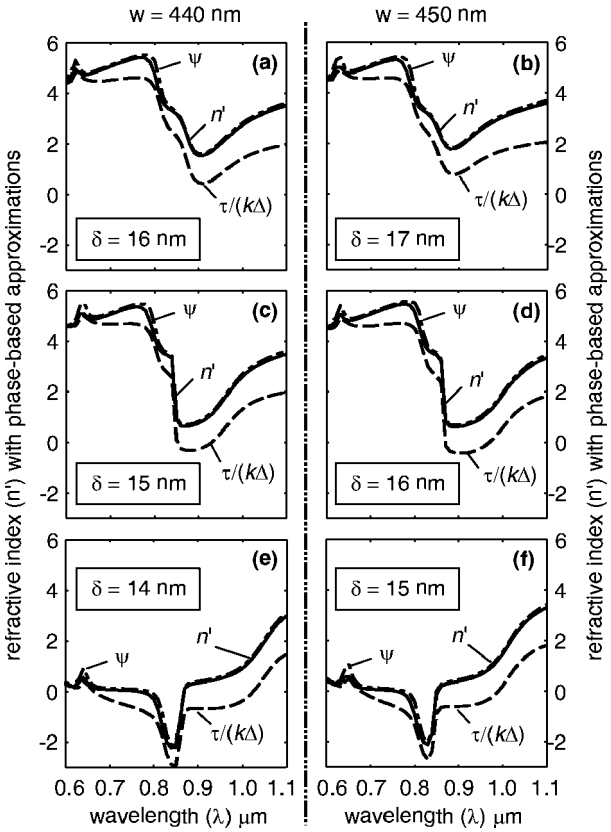

Fig. 5. Refractive index of periodic paired strips obtained for six different geometries from FEM simulations and approximations at the same wavelength range. (a), (c), and (e) Strips are 440 nm wide; (b), (d), and (f), strips are 450 nm wide. Approximating function Ψ is given by expression (17).

from a wavelength of 2.5 μm (not shown) and then continues toward smaller values with a gradual step-size variation from 50 to 1 nm at steep segments. The cases of Fig. 5 are specifically selected to represent the main possible scenarios, i.e., positive refraction, shown in Figs. 5(a) and 5(b); negative refraction, shown in Figs. 5(e) and 5(f); or a transition to $n'<1$, shown in Figs. 5(c) and 5(d).

Notice that expressions (16) and (17) do not include either $|t|$ or $|r|$ and suggest an instrumental role for phase differences $\tau=\arg t$ and $\rho=\arg r$ in representing NIM features. Indeed, in all cases, both approximations illustrate well the changes of n'. Certainly, the approximate formula of expression (17) works better than the simpler formula of expression (16). This is because the reflection is quite large at short waves, and it is increasing toward longer wavelengths, as shown in Fig. 4(c).

D. High-precision Phase Measurements of Thin NIMs

We performed phase measurements by using polarization and walk-off interferometry schemes depicted in Fig. 6 for transmitted light phases (τ). The phase differences in reflection (ρ) are measured in a similar manner. In both schematic diagrams, LC is a liquid-crystal phase compensator, PD is a photodetector, and P is a linear polarizer (the axes of the input–output polarizers are parallel at 45°).

In the polarization interferometer shown in Fig. 6(a), the two optical channels have a common geometrical path and differ only by the polarization of light. The phase differences caused by anisotropy of a refractive material in transmission $\Delta\tau$ (or reflection $\Delta\rho$) are measured between orthogonally polarized waves $\Delta\tau=\tau_{\parallel}-\tau_{\perp}$ (or $\Delta\rho=\rho_{\parallel}-\rho_{\perp}$). Notice that the phase acquired in the substrate contributes nothing to either $\Delta\tau$ or $\Delta\rho$.

The walk-off interferometer, shown in Fig. 6(b), has two optical channels that differ in geometrical path; this yields a phase shift introduced by a NIM sample in transmission (τ_s) or reflection (ρ_s) relative to a reference (τ_{air} or ρ_{air}) so that $\delta\tau=\tau_s-\tau_{\text{air}}$ or $\delta\rho=\rho_s-\rho_{\text{air}}$. A layer of air with the same thickness as the NIM layer is used as the reference. Both the reference and the sample beams go through the substrate so that the phase acquired in the substrate does not contribute to the measured phase shift $\delta\tau$ and $\delta\rho$, provided that the substrate has no deviations in optical thickness. The walk-off effect in anisotropic crystals (ACs) is employed to separate the two beams and then bring them together to produce interference. The phase shifts $\delta\tau_{\parallel}(\delta\rho_{\parallel})$ and $\delta\tau_{\perp}(\delta\rho_{\perp})$ are measured for two light polarizations by using a set of diode lasers and a tunable erbium laser, and their difference is compared with the phase anisotropy $\Delta\tau(\Delta\rho)$ obtained from polarization interferometry, since $\Delta\tau=\delta\tau_{\parallel}-\delta\tau_{\perp}$ and $\Delta\rho=\delta\rho_{\parallel}-\delta\rho_{\perp}$.

The instrumental error of the phase anisotropy measurement by the polarization interferometer is ±1.7°. We note that variations in the substrate thickness do not affect the results of our phase anisotropy measurements, which is typical for common-path interferometers. In the case of the walk-off interferometer, the thickness variation gives an additional source of error, causing the error for the absolute phase-shift measurements to increase up to ±4°.

As shown in expression (16), in the case of low reflection and small thickness, Eq. (6) confines the phase difference to $|\tau|\approx 2\pi n'\Delta/\lambda$, so that $n'<0$ results in $\tau<0$. In experiments using interferometry, the phase shift due to a

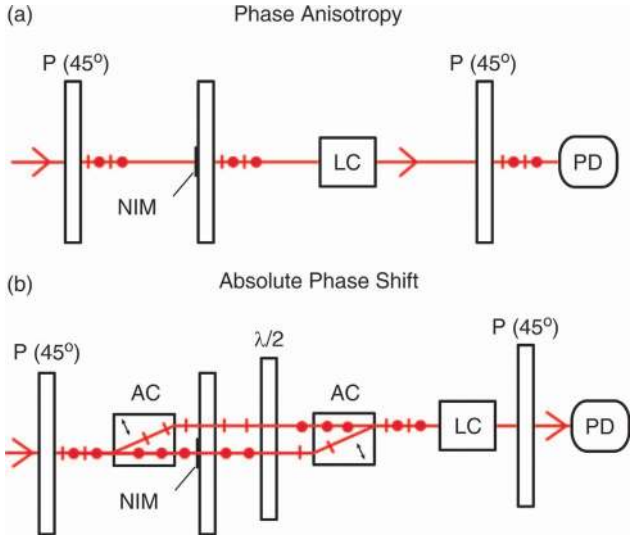

Fig. 6. Schematics of (a) polarization and (b) walk-off interferometers for measuring phase anisotropy and absolute phase induced by a NIM sample. LC is a liquid-crystal phase compensator, P is 45-deg linear polarizer, AC is an anisotropic calcite crystal with a walk-off effect, $\lambda/2$ is a half-wave plate, and PD is a photodetector.

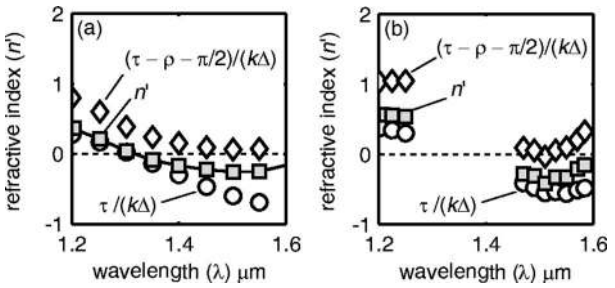

Fig. 7. Refractive index of a NIM layer restored from (a) FDTD simulations and (b) measurements. Approximations in both cases are obtained using expressions (16) and (17).

NIM layer can be precisely measured relative to a layer of air of the same thickness: $\tau_{\mathrm{exp}}=\tau-\tau_{\mathrm{air}}$, where the phase shift in air is a reference phase, $\tau_{\mathrm{air}}=2\pi\Delta/\lambda$. Then n' is negative in the material, provided that $\tau_{\mathrm{exp}}<-\tau_{\mathrm{air}}$. In general, for a NIM layer with reflection, one should also account for ρ as in expression (17). In materials with strong absorption, the relation between complex parameters t, r, and n is even more complicated, and phase measurements should be accompained by measurements of the transmittance and reflectance magnitudes in order to use the accurate procedure of Eqs. (10)–(12).

To validate the procedure for the restoration of n' and the phase-based approximations [expressions (16) and (17)], we use experimental data of our 3D NIM sample[22] (see Subsection 3.C for more detailed consideration of this sample B, consisting of pairs of coupled nanorods). The sample is arranged of a periodic array of coupled gold nanorods deposited directly on glass. Figure 7 shows the refractive index obtained (a) from FDTD simulations and (b) from measurements. A segment of the wavelength range in which the refractive index becomes minimal is selected. The minimal value of n' for this structure is about −0.3 at 1.5 μm. In contrast to the examples of Fig. 5, in this case approximations by expression (16) work better to owing lower reflection.

3. NUMERICAL AND PHYSICAL EXPERIMENTS WITH NIMS

Up to now, we have seen that a negative refractive index is provided by resonant coupled metal–dielectric elementary scatterers. For example, our typical models of Fig. 4(a) display negative refraction up to $n=-2$, as shown in Figs. 4(d), 5(e), and 5(f). These strip structures can be readily fabricated, but losses are still rather large.

We now analyze the NIM–substrate interaction, beginning with the basic cases of a single gold rod on ITO–glass and pure glass substrates. We then consider several core 3D NIMs that demonstrate a negative refractive index proven in both experiments and simulations.[22–24]

A. Equivalent Debye Model in FDTD

Rather than utilizing the previously applied FEM to investigate the resonance behavior of gold strips and to pinpoint a negative refractive index as an effective quantity, we use for 3D structures a numerical method involving the well-known finite-difference time-domain (FDTD) technique.[28] The FDTD modeling of plasmonic resonances in the optical range is more complicated than either a standard perfect electric conductor approach for thin skin depths or a direct application of conductivity.

The Drude model for a given single decay constant (Γ) and plasma frequency (ω_p) is defined as[29]

$$\varepsilon_r(\omega)=\varepsilon_\infty-\frac{\omega_p^2}{\omega(\omega+i\Gamma)}, \tag{18}$$

and the equivalent Debye model is defined as

$$\varepsilon_r(\omega)=\varepsilon_\infty+\frac{\chi_1}{1-i\omega t_0}-\frac{\sigma}{i\omega\varepsilon_0}, \tag{19}$$

where ε_∞ is the permittivity at infinite frequencies, $\chi_1=\varepsilon_s-\varepsilon_\infty$ is the permittivity step, and $t_0=1/\Gamma$ is the relaxation time. Note that the Debye model can be straightforwardly derived from the Drude model [Eq. (18)] by using a partial fraction expansion; this gives $\chi_1=-(\omega_p t_0)^2$ and $\sigma=\omega_p^2\varepsilon_0 t_0$.

Using Eq. (19) in $\mathbf{D}=\varepsilon(\omega)\mathbf{E}$, we obtain $\mathbf{D}(\omega)=\varepsilon_0[\varepsilon_\infty\mathbf{E}+\mathbf{I}_1(\omega)+\mathbf{I}_2(\omega)]$, where

$$\mathbf{I}_1(\omega)=\frac{\chi_1}{1-i\omega t_0}\mathbf{E}(\omega), \tag{20}$$

$$\mathbf{I}_2(\omega)=-\frac{\sigma}{i\omega\varepsilon_0}\mathbf{E}(\omega). \tag{21}$$

Separating each term in the time domain, we introduce a new displacement current vector $\mathbf{D}(t)=\varepsilon_0[\varepsilon_r\mathbf{E}+\mathbf{I}_1(t)$

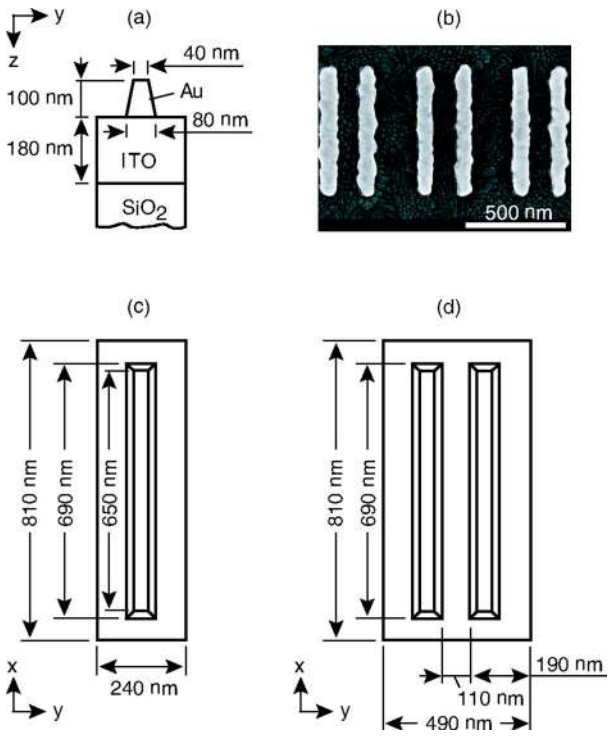

Fig. 8. (a) and (c), Single-periodic and (b) and (d) double-periodic models for numerical simulations of noncoupled rods deposited on an ITO–glass or bare glass substrate. Geometry in (b) and (d) represents sample A fabricated by electron-beam lithography.

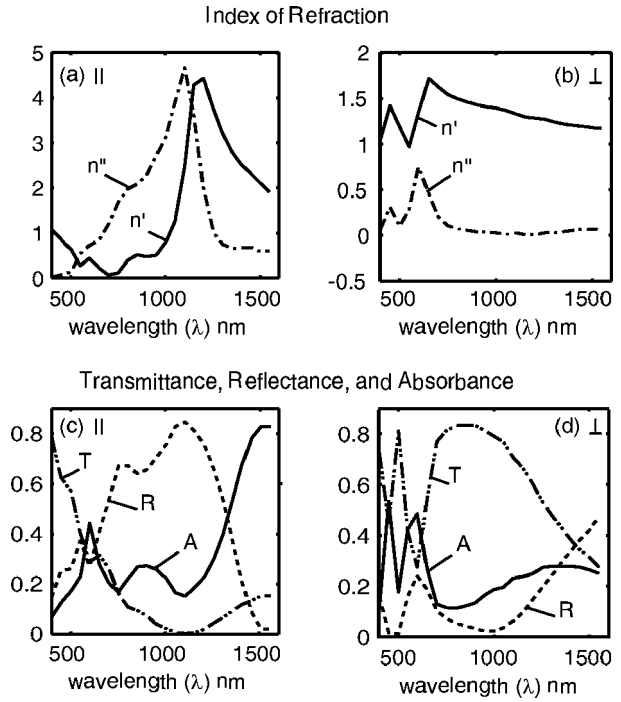

Fig. 9. Index of refraction for (a) parallel, and (b) perpendicular polarizations of incident light obtained from FDTD simulations with the geometry of Figs. 8(a) and 8(c). (c) and (d) Transmittance (T), reflectance (R), and absorbance (A) calculated for the same polarizations.

$+\mathbf{I}_2(t)]$, where the time-domain versions of Eqs. (20) and (21) are defined by the following convolutions:

$$\mathbf{I}_1(t) = -\omega_p{}^2 t_0 \int_0^t \exp[-(t-\tau)/t_0] E(\tau) \mathrm{d}\tau, \tag{22}$$

$$\mathbf{I}_2(t) = \omega_p^2 t_0 \int_0^t \mathbf{E}(\tau) \mathbf{d}\tau. \tag{23}$$

Then, except for a new integration term $[\mathbf{I}_1(t)]$, the calculation scheme is similar to the standard eddy current problem.[28]

B. Noncoupled Nanorods on an ITO–Glass or Bare Glass Substrate

Consider, for example, FDTD modeling of the periodic metal–dielectric structure shown in Figs. 8(a) and 8(c). The elementary cell of the array is made up of a single gold nanorod placed on an ITO–glass substrate. The restored values of the refractive index [using Eq. (15) and then Eqs. (10)–(12)] are shown in Fig. 9 for (a) parallel and (b) perpendicular polarizations of the incident light. Transmittance (T), reflectance (R), and absorbance (A) are also calculated for the same model with parallel and perpendicular polarizations [Figs. 9(c) and 9(d), respectively].

The basic single structure creates an almost zero-equivalent refractive index, demonstrates resonant absorbance for the parallel polarization, and displays a completely different behavior for the other polarization direction. (Following characteristic dimensions, resonant features for perpendicular polarizations are shifted toward much shorter wavelengths.) On obtaining the result, we suggest that for the transverse magnetic case, where the electric field is parallel to the periodic rods, we observe a coupled resonant behavior because, as shown below, the electric field is able to circulate in continuous contours at the rod–substrate interface. We also imply that strong coupling with a lossy substrate such as ITO could be unfavorable. For this reason, a novel, to our knowledge, double-periodic structure has been fabricated, tested, and simulated using a 3D FDTD code.

A scanning electron microscope (SEM) image of the new, double-periodic structure (called sample A) is shown in Fig. 8(b), and a top view of the unit cell is shown in Fig. 8(d). The double-periodic structure consists of two rods that share the dimensions of the single rod in Figs. 8(a) and 8(c). We note that, in spite of more sophisticated periodicity, the double-periodic metallic elements exhibit similar refractive index behavior and absorbance in both polarization directions. An example for the parallel polarization is shown in Figs. 10(a) and 10(c). That also suggests that deviations (up to 20%) in periodicity do not change the equivalent optical properties of the periodic

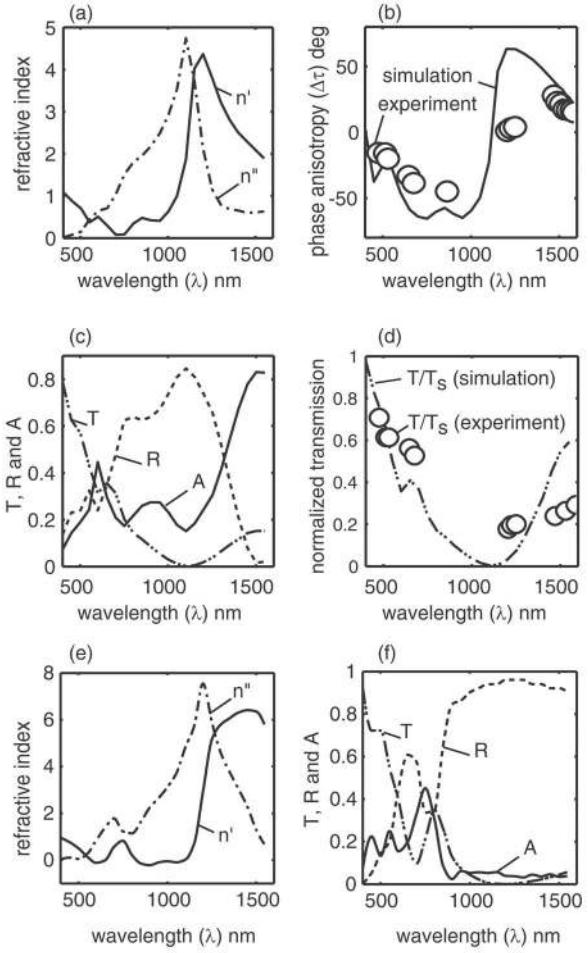

Fig. 10. (a) Index of refraction for parallel polarization and (b) the phase anisotropy in transmission obtained from FDTD simulations with the geometry of Figs. 8(b) and 8(d). (c) Transmittance (T), reflectance (R), and absorbance (A) calculated for the same polarization. (d) Calculated values of the normalized transmission (T/T_s) are compared with the experimental data. (e) The refractive index for the identical composite structure but without any background. (f) T, R, and A for this case.

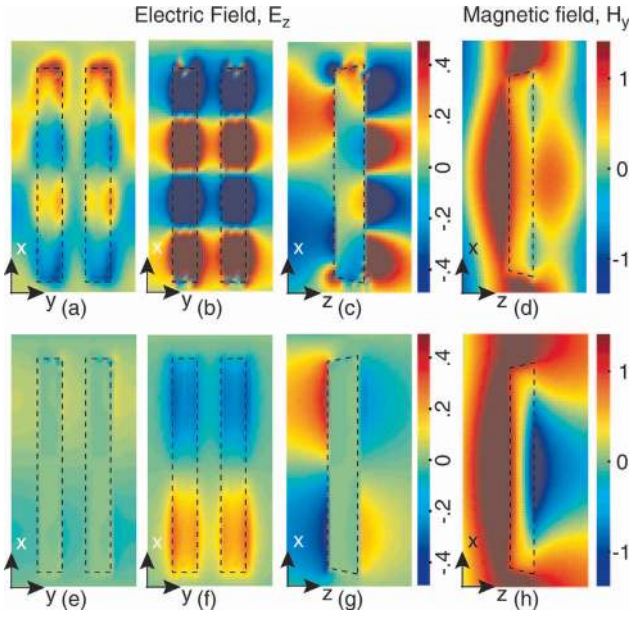

Fig. 11. (a)–(d) Field maps for noncoupled rods on an ITO–glass substrate. (e)–(h) Similar maps for the sample without any background. In (a) and (e) electric field component E_z is mapped at xy cross sections, through the middle of the rod; in (b) and (f), just 10 nm beyond the rod inside ITO. E_z in (c) and (g) and H_y in (d) and (h) are mapped at the xz cross section through the middle of the rod. All magnetic field values are normalized by the magnetic incident field taken at the geometrical center of the rod.

plasmonic structure. We note that in spite of the nonidealities of sample A, shown in Fig. 8(a), both the phase anisotropy in Fig. 10(b) and the transmittance (T) normalized by the transmittance of the substrate (T_s) in Fig. 10(d) satisfactorily match the experimental data.

As illustrated below, the rods are also coupled inductively to the ITO–glass substrate. The electric field component E_z, which is not mixed with the incident field, is mapped at xy cross sections taken through the middle of the rod [see Fig. 11(a)] and just 10 nm beyond the rod inside the ITO [Fig. 11(b)]. The rods are shown by dashed lines in Fig. 11. In both cases the two rods perform almost like a strip, forming a high-order evanescent mode inside ITO. In addition to xy cross-sectional field maps, Fig. 11 depicts the values of the electric field component E_z in Fig. 11(c) and magnetic field component H_y in Fig. 11(d) mapped at xz cross sections through the middle of the rod. The values of H_y are normalized by the incident magnetic field taken at the geometrical center of the rod.

The losses in ITO are large enough to allow for electric fields to circulate along continuous contours through the gold–ITO interface. After the incident magnetic field is added to the induced one, reversed magnetic field zones are observed right at the gold–ITO interface [see Fig. 11(d)].

With FDTD analysis of noncoupled rods of Fig. 8(d), it was discovered that a simple substitution of the ITO–glass substrate with bare glass could provide a negative refractive index. Figure 10(e) depicts FDTD results for the noncoupled rods of Fig. 8(d) but without any substrate. The minimal value of $n' \approx -0.2$ is achieved at a wavelength of 0.9 μm. The results are consistent with the more intense and larger field reversal zone shown in Fig. 11(h). We note a substantially different distribution of the electric component E_z in this case. This observation of negative refractive index for single, noncoupled rods is in agreement with earlier theoretical predictions.[19]

C. Sample B: Coupled Nanorods on a Bare Glass Substrate

In addition to results for single, planar, noncoupled rods, 3D coupled rods[18–22] with a magnetic field reversal similar to that above would be desirable. Such a NIM would consist of periodic arrays of coupled gold rods oriented parallel to the incident electric field and deposited directly on glass. An example unit cell is depicted in Figs. 12(a) and 12(c), and the results for the refractive index and transmittance, reflectance, and absorbance are shown in Figs. 13(a) and 13(b). The model demonstrates a refractive index of about −0.5 at 1360 μm, although with substantial losses around this point.

To avoid a probable interaction between the rows of coupled rods, and to possibly decrease losses, an alternative sample (sample B) with a skewed symmetry as shown in Figs. 12(b) and 12(d) has been manufactured and simulated. Sample B requires a unit cell four times larger than that considered for the structure of Figs. 12(a) and 12(c),

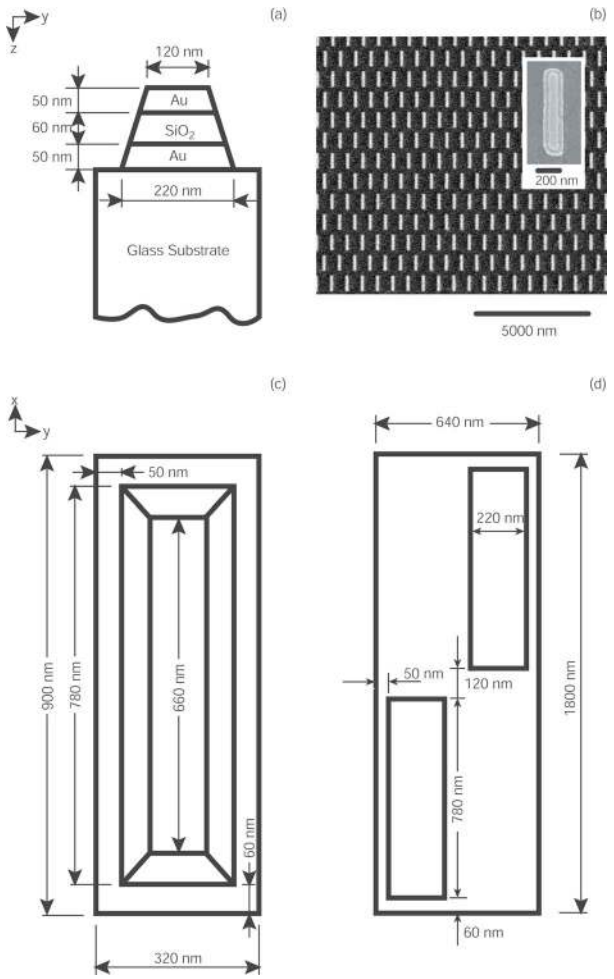

Fig. 12. (c) Single-periodic and (d) skewed-periodic structures of coupled gold rods deposited on a bare glass substrate. Both models used the same rod pairs shown in (a). Geometry in (d) simulates a fabricated sample (sample B). (b) SEM image of sample B.

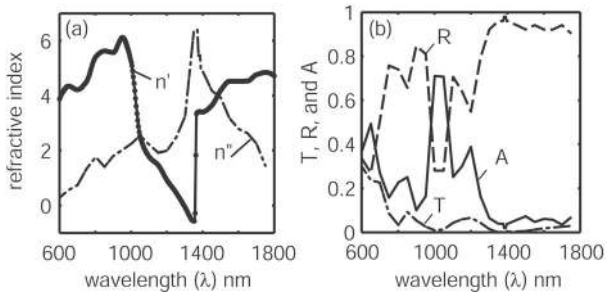

Fig. 13. (a) Index of refraction for parallel polarization of incident light obtained from FDTD simulations with the geometry of Fig. 12(a). (b) Simulated transmittance (T), reflectance (R), and absorbance (A) for parallel polarization.

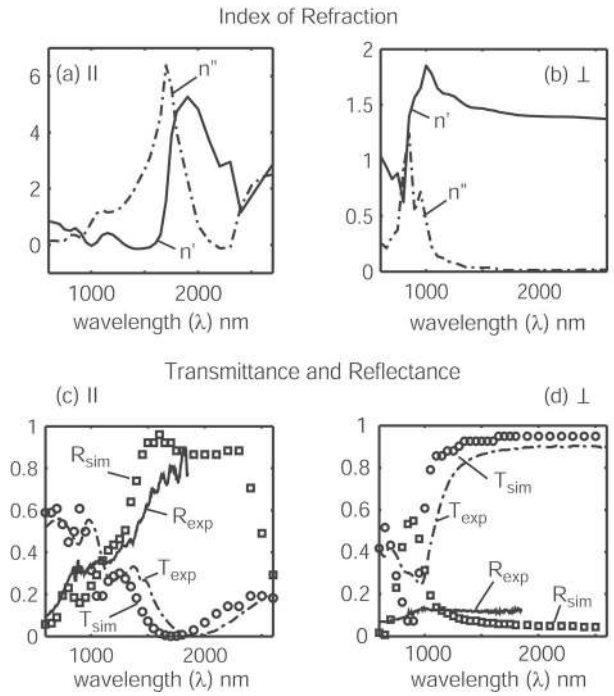

Fig. 14. Index of refraction for (a) parallel and (b) perpendicular polarizations of incident light obtained from FDTD simulations with the geometry of Figs. 8(b) and 8(d). (c) and (d) Simulated and experimental transmittance (T_{sim} and T_{exp}) and reflectance (R_{sim} and R_{exp}) calculated for the same polarizations.

and, consequently, one would expect a weaker negative-refraction effect due to a smaller metal filling factor. Indeed, as shown in Fig. 14(a), the index of refraction obtained from FDTD simulations for parallel polarization is −0.2 at 1.5 μm with the geometry of Figs. 12(b) and 12(d). Experimental studies of the NIM provide a value of $n = -0.3 \pm 0.1$ at 1.5 μm[22] (see also Fig. 7 above). Both the experimental and the simulated values of the refractive index have already been compared with phase-only approximations in Fig. 7. Simulated and experimental transmittance (T_{sim} and T_{exp}) and reflectance (R_{sim} and R_{exp}) calculated for the same polarizations are shown in Figs. 14(c) and 14(d).

Direct deposition of the gold nanorod pairs on a bare glass substrate eliminates the damping effect from the ITO layer, and larger magnetic reactions are attainable owing to this fabrication method. For testing our assumptions on the effect of an ITO–glass substrate on NIM properties, we have fabricated a preliminary sample on an ITO–glass substrate with a geometry close to that of sample B and compared it with the results from sample B.

First, in contrast to sample B, the preliminary sample does not demonstrate a negative refractive index in either experiment or simulations. Second, the induced electric mode between the rods appears to be too high, and the magnitude of the induced magnetic dipole moment is too low for a good magnetic reaction in this case. That effect is illustrated in Fig. 15. The figure shows simulated maps of the electric field E_z obtained for the two samples with similar geometries. Field maps in Figs. 15(a) and 15(b) represent the sample deposited on an ITO–glass substrate, and the maps in Figs. 15(c) and 15(d) are calculated for the same geometry deposited on bare glass (sample B). E_z is taken at two xy cross sections, first through the middle of the rod, as shown in Figs. 15(a) and 15(c), and then at 10 nm beyond the rod inside the substrate, as depicted in Figs. 15(b) and 15(d). Comparison of Figs. 15(a) and 15(c) allows us to conclude that the elimination of ITO produces stronger current in the required mode between the rods. Weaker higher-order current modes are generated between the rods in the sample with an ITO–glass substrate, as shown in Fig. 15(a).

In addition, both samples are not optimized for the best magnetic reaction, since the second rod in both cases does not channel a sufficient part of the electric field. Indeed, we have assumed that E_z should be at least weaker (or reversed) just beyond the second rod. Unfortunately, in both samples, as indicated in Figs. 15(b) and 15(d), E_z neither decays nor changes its direction at the cross section just behind the rods. In essence, the presence of any substrate alters the symmetry of the interacting rods and restrains the magnetic reaction between the rod pair. This defect could be alleviated by one's optimizing the design of the structure.

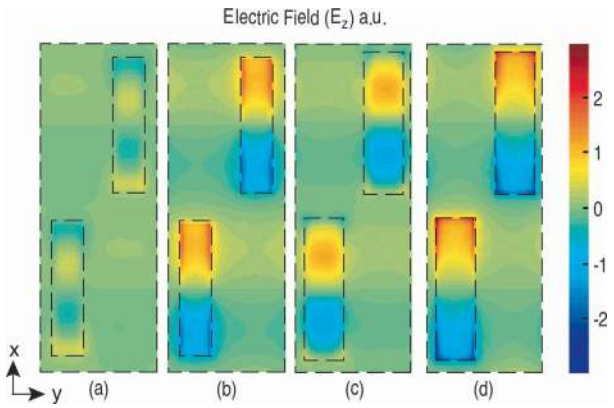

Fig. 15. Simulated maps of E_z obtained for two samples. (a) and (b) Field maps are calculated for the sample deposited on an ITO–glass substrate; (c) and (d) field maps are calculated for a similar sample deposited on bare glass (sample B). Electric field (E_z) is mapped at two xy cross sections: through the middle of the rod, as in (a) and (c), or just 10 nm beyond the rod inside, ITO or glass, as in (b) and (d).

D. Inverted Nanorods: Coupled Elliptic Voids in Metallic Films

To achieve a NIM within a given range of optical wavelengths, one could also employ an inverted structure along with dielectric spacers between coupled metallic elements. Such a design offers a good manufacturability for a thick multilayer NIM.

An FDTD model is created to match the experimental sample of Ref. 24; the dimensions used in simulations are rounded (shown in parentheses). The basis of the structure consists of a three-layer film composite deposited over a BK7 glass substrate. The composite consists of two 30 (30) nm layers of gold separated by a 75 (80) nm layer of Al_2O_3 as shown in Fig. 16(a). An array of elliptical wells (voids) is then etched out of the three-layer composite to give the final sample with a 2D lattice period of 787 (790) nm. The dimensions of the elementary cell with the well are depicted in Figs. 16(a) and 16(b). A midsection view of the elementary cell along the short axis of the elliptic well is shown in Fig. 16(a).

Figure 17 shows the simulated index of refraction for (a) parallel and (b) perpendicular polarizations of incident light for the geometry of Fig. 16 together with phase-based approximations by expressions (16) and (17). Transmittance (T), reflectance (R), and absorbance (A) are shown in Figs. 17(c) and 17(d). As expected, a simple approximation with expression (16) works well in the case of moderate reflection [see Figs. 17(a) and 17(c)] in comparison with the case of large R [see Figs. 17(b) and 17(d)]. The other approximation, expression (17), provides a better fit in all cases.

The inverted NIM demonstrates a negative refractive index of −1.5 at 1.8 μm for perpendicular polarization (the electric field is along the short axis of the elliptic well) and −0.75 at 1.6 μm for parallel polarization (the electric field is along the long axis of the elliptic well), which is consistent with the experimental data.[24] As expected for inverted structures, the perpendicular polarization works better than the parallel one.

4. SUMMARY

We have described and discussed several thin composite metal–dielectric structures that demonstrate an effective negative refractive index. We considered examples of how the complex values of the transmission and reflection coefficients (t and r) taken from either measurements or simulations could be used to obtain the index of refraction. From t and r for the incident plane wave, we calculated the effective refractive index for all the composite materials considered herein. The description is based on an effective layer of homogeneous media with the same effect on t and r as a given layer of a NIM of the same thickness. Characteristic matrices are used to obtain the effective impedance and the effective refractive index for a single unknown NIM layer in an arbitrary multilayer structure.

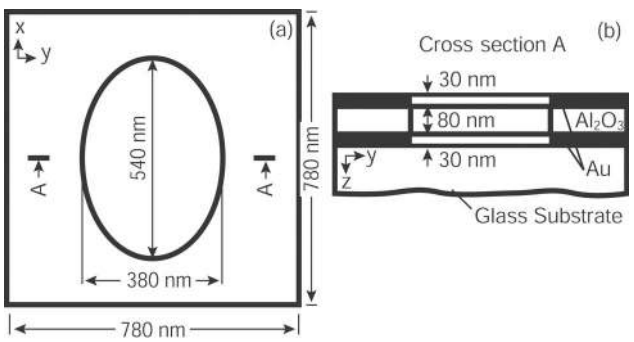

Fig. 16. (a) Elementary cell of coupled elliptic voids as an inversion of coupled nanorods. (b) A cross-sectional view of the elementary cell shown in (a).

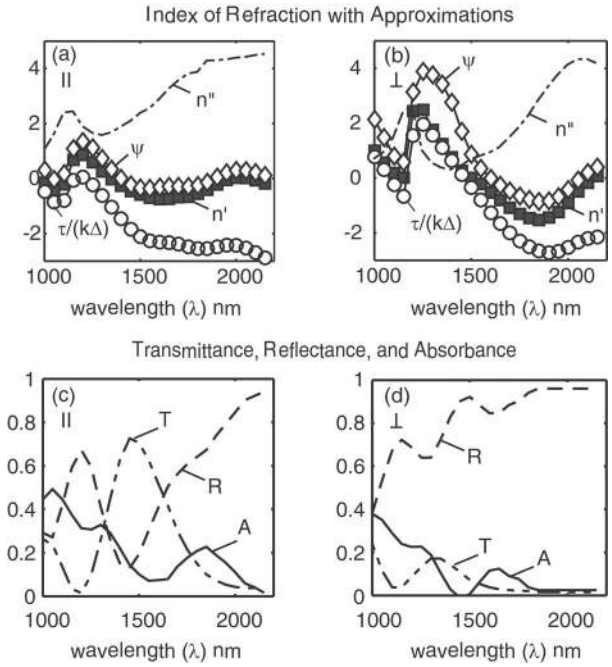

Fig. 17. Index of refraction for (a) parallel polarization, and (b) perpendicular polarization of incident light is obtained from simulations for the inverted geometry of Figs. 16(a) and 16(b). Approximations with expressions (16) and (17) are also tested for the inverted geometry. Transmittance (T), reflectance (R), and absorbance (A) calculated for the same polarizations are shown in (c) and (d).

Our simulations show that a composite NIM based on a 2D periodic array of coupled gold strips separated by a continuous dielectric layer can have a negative refractive index to −2.

We also showed the critical importance of phases for retrieval of the refractive index. We have found that formulas using only the phases of t and r could represent a good alternative to exact restoration of the refractive index. Consequently, we propose two interferometry schemes: the polarization interferometer for measuring phase anisotropy between two different polarizations in transmission (reflection) and the walk-off interferometer for measuring absolute phases.

We found that noncoupled gold rods arranged on an ITO–glass substrate do not provide a negative refractive index because of the damping associated with the conductive features of ITO. We deduce that losses in ITO introduce a barrier to achieving negative refraction with ITO–glass substrates. Simulations indicate that an identical structure on a glass substrate could give $n' \approx -0.2$.

Experimental studies for a sample based on an array of paired metal rods on a glass substrate allowed us to ob-

serve a negative refractive index of −0.3 at 1.5 μm, in good agreement with our simulations.

Finally, we showed that inverse structures also provide good results in creating NIMs. We analyzed an inversion of the coupled rods' structure, in which the coupled gold rods were replaced by coupled voids in gold films. Validating the design suggested in Ref. 24, we obtained refractive indices of −1.5 at 1.8 μm for perpendicular polarization (the electric field along the short axis of the elliptic well) and −0.75 at 1.6 μm for parallel polarization. Again, using our suggested phase-based approximations, we found that, similar to noninverted designs, only the phases of t and r are sufficient to provide estimates of the negative refraction effect in inverted designs with voids.

We expect that further optimization of design techniques for composite NIMs will provide a stronger effect at smaller losses, enabling new devices based on scalable 3D NIM structures.

This work was supported in part by U. S. Army Research Office grant W911NF-04-1-0350 and by National Science Foundation, Nanoscale Interdisciplinary Research Teams award ECS-0210445. Corresponding author V. M. Shalaev can be reached by e-mail at shalaev@ecn.purdue.edu.

*Present address, Ethertronics Inc., 9605 Scranton Road, San Diego, California 92121.

REFERENCES

1. L. I. Mandel'shtam, "Group velocity in crystal lattice," JETP **15**, 475 (1945). See also Ref. 2.
2. L. I. Mandel'shtam, "The 4th lecture of L. I. Mandel'shtam given at Moscow State University (05/05/1944)," in *Collection of Scientific Works* (Nauka, 1994), Vol. 5, pp. 461–467.
3. V. G. Veselago, "The electrodynamics of substances with simultaneously negative values of ε and μ," Sov. Phys. Usp. **10**, 509–514 (1968).
4. H. Lamb, "On group-velocity," Proc. London Math. Soc.1, 473–479 (1904).
5. A. Schuster, *An Introduction to the Theory of Optics* (Edward Arnold, 1904).
6. J. B. Pendry, "Negative refraction makes a perfect lens," Phys. Rev. Lett. **85**, 3966–3969 (2000).
7. V. A. Podolskiy and E. E. Narimanov, "Near-sighted superlens," Opt. Lett. **30**, 75–77 (2005).
8. K. J. Webb, M. Yang, D. W. Ward, and K. A. Nelson, "Metrics for negative-refractive-index materials," Phys. Rev. E **70**, 035602(R) (2004).
9. N. A. Khizhnyak, "Artificial anisotropic dielectrics formed from two-dimensional lattices of infinite bars and rods," Sov. Phys. Tech. Phys. **29**, 604–614 (1959).
10. A. N. Lagarkov and A. K. Sarychev, "Electromagnetic properties of composites containing elongated conducting inclusions," Phys. Rev. B **53**, 06318 (1996).
11. T. J. Yen, W. J. Padilla, N. Fang, D. C. Vier, D. R. Smith, J. B. Pendry, D. N. Basov, and X. Zhang, "Terahertz magnetic response from artificial materials," Science **303**, 1494–1496 (2004).
12. S. Linden, C. Enkrich, M. Wegener, J. Zhou, T. Koschny, and C. Soukoulis, "Magnetic response of metamaterials at 100 terahertz," Science **306**, 1351–1353 (2004).
13. S. Zhang, W. Fan, B. K. Minhas, A. Frauenglass, K. J. Malloy, and S. R. J. Brueck, "Midinfrared resonant magnetic nanostructures exhibiting a negative permeability," Phys. Rev. Lett. **94**, 037402 (2005).
14. A. K. Sarychev and V. M. Shalaev, "Magnetic resonance in metal nanoantennas," in *Complex Mediums V: Light and Complexity*, M. W. McCall and G. Dewar, eds., Proc. SPIE **5508**, 128–137 (2004).
15. C. Enkrich, M. Wegener, S. Linden, S. Burger, L. Zschiedrich, F. Schmidt, J. Zhou, Th. Koschny, and C. M. Soukoulis, "Magnetic metamaterials at telecommunication and visible frequencies," arXiv: cond-mat/0504774v1, Apr. 29, 2005.
16. A. Berrier, M. Mulot, M. Swillo, M. Qiu, L. Thylén, A. Talneau, and S. Anand, "Negative refraction at infrared wavelengths in a two-dimensional photonic crystal," Phys. Rev. Lett. **93**, 073902 (2004).
17. E. Schonbrun, M. Tinker, W. Park, and J.-B. Lee, "Negative refraction in a Si-polymer photonic crystal membrane," IEEE Photon. Technol. Lett. **17**, 1196–1198 (2005).
18. V. A. Podolskiy, A. K. Sarychev, and V. M. Shalaev, "Plasmon modes in metal nanowires and left-handed materials," J. Nonlinear Opt. Phys. Mater. **11**, 65–74 (2002).
19. V. A. Podolskiy, A. K. Sarychev, and V. M. Shalaev, "Plasmon modes and negative refraction in metal nanowire composites," Opt. Express **11**, 735–745 (2003).
20. V. A. Podolskiy, A. K. Sarychev, E. E. Narimanov, and V. M. Shalaev, "Resonant light interaction with plasmonic nanowire systems," J. Opt. A Pure Appl. Opt. **7**, S32–S37 (2005).
21. A. K. Sarychev, V. P. Drachev, H.-K. Yuan, V. A. Podolskiy, and V. M. Shalaev, "Optical properties of metal nanowires," in *Nanotubes and Nanowires*, A. Lakhtakia and S. Maksinenku, eds., Proc. SPIE **5219**, 92–98 (2003).
22. V. M. Shalaev, W. Cai, U. Chettiar, H.-K. Yuan, A. K. Sarychev, V. P. Drachev, and A. V. Kildishev, "Negative index of refraction in optical metamaterials," Opt. Lett. **30**, 3356–3358 (2005).
23. S. Zhang, W. Fan, N. C. Panoiu, K. J. Malloy, R. M. Osgood, and S. R. J. Brueck, "Demonstration of near-infrared negative-index materials," arXiv: physics/0504208.
24. S. Zhang, W. Fan, K. J. Malloy S. R. J. Brueck, N. C. Panoiu, and R. M. Osgood, "Demonstration of metal–dielectric negative-index metamaterials with improved performance at optical frequencies," J. Opt. Soc. Am. B **23**, 434–438 (2006).
25. J. D. Jackson, *Classical Electrodynamics* (Wiley, 1962), p. 291.
26. Y. Svirko, N. Zheludev, and M. Osipov, "Layered chiral metallic microstructures with inductive coupling," Appl. Phys. Lett. **78**, 498–500 (2001).
27. D. R. Smith, S. Schultz, P. Markoŝ, and C. M. Soukoulis, "Determination of effective permittivity and permeability of metamaterials from reflection and transmission coefficients," Phys. Rev. B **65**, 195104 (2002).
28. A. Taflove and S. Hagness, *Computational Electrodynamics: The Finite-Difference Time-Domain Method* (Artech House, 2000).
29. A. Ishimaru, *Electromagnetic Wave Propagation, Radiation, and Scattering* (Prentice Hall, 1991).